

Article

One-Step Synthesis of High-Efficiency Oxygen Evolution Reaction Catalyst FeS_x(Y/MB) with High Temperature Resistance and Strong Alkali

Jing Wang, Lingling Feng, Zikang Zhao, Yan Wang, Ying Zhang, Shan Song, Shengwei Sun, Junshuang Zhou * and Faming Gao *

Hebei Key Laboratory of Applied Chemistry, School of Environmental and Chemical Engineering, Yanshan University, Qinhuangdao 066004, China

* Correspondence: jszhou@ysu.edu.cn (J.Z.); fmgao@ysu.edu.cn (F.G.)

Abstract: Given the energy crisis and escalating environmental pollution, the imperative for developing clean new energy is evident. Hydrogen has garnered significant attention owing to its clean properties, high energy density, and ease of storage and transportation. This study synthesized four types of catalysts—FeS(DI/MB), FeS(ET/MB), Fe(DI/MB), and Fe(ET/MB)—using two distinct solution systems: DI/MB and ET/MB. The FeS(DI/MB) catalyst, synthesized using the layered solution system (DI/MB), demonstrates a uniformly distributed and dense nanosheet structure, exhibiting excellent resistance to strong bases and superior catalytic properties. The FeS(DI/MB) electrode showed OER overpotentials of 460 mV and 318 mV in 1 M and 6 M, respectively, at current densities of up to 500 mA cm⁻². Under industrial electrolysis test conditions, the FeS(DI/MB) electrode required only 262 mV to achieve a current density of 500 mA cm⁻², operating in a high-temperature, strong alkaline environment of 6 M at 60 °C. Furthermore, the FeS(DI/MB) electrode exhibited excellent OER catalytic activity and stability, as evidenced by a 60 h stability test. These findings provide valuable insights into the preparation of iron nickel sulfide-based catalysts, and further in-depth and comprehensive exploration is anticipated to yield the excellent catalytic performance of these catalysts in the realm of electrolytic water hydrogen production.



Citation: Wang, J.; Feng, L.; Zhao, Z.; Wang, Y.; Zhang, Y.; Song, S.; Sun, S.; Zhou, J.; Gao, F. One-Step Synthesis of High-Efficiency Oxygen Evolution Reaction Catalyst FeS_x(Y/MB) with High Temperature Resistance and Strong Alkali. *Catalysts* **2024**, *14*, 324. <https://doi.org/10.3390/catal14050324>

Academic Editor: Akira Nishimura

Received: 27 March 2024

Revised: 11 May 2024

Accepted: 14 May 2024

Published: 16 May 2024



Copyright: © 2024 by the authors. Licensee MDPI, Basel, Switzerland. This article is an open access article distributed under the terms and conditions of the Creative Commons Attribution (CC BY) license (<https://creativecommons.org/licenses/by/4.0/>).

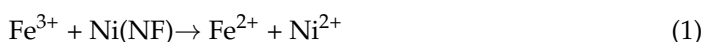
Keywords: OER; iron–nickel sulfide catalysts; nanomaterials

1. Introduction

Hydrogen, as an ideal clean energy source, is in increasing demand. Currently, hydrogen production from electrolyzed water is the most important method [1]. Due to the reaction mechanism, the oxygen evolution reaction (OER) controls the process of electrolyzed water [2,3]. Thus, finding efficient and stable OER catalysts is necessary to enhance the efficiency of hydrogen production [4,5]. For ease of comparison, the academic community typically selects the oxygen evolution overpotential (η) corresponding to a current density (j) of 10 mA cm⁻² to assess the catalyst's catalytic performance [6]. A current density (j) of 10 mA cm⁻² equates to the minimum current density required for water decomposition achievable by solar water electrolysis equipment operating at 10% efficiency under standard sunlight intensity, significantly lower than that needed for industrial hydrogen production. The increase in current density affects the catalytic performance of the material, making it of great significance for industrial production that the catalyst material maintains high-efficiency catalytic activity even under high-current conditions [7]. In testing the electrochemical performance of hydrogen evolution and oxygen evolution catalysts, laboratories commonly use 1 M KOH as the electrolyte [8,9]. Nonetheless, testing hydrogen and oxygen evolution reactions in a 1 M KOH electrolyte leads to higher overpotential, hindering the water electrolysis process, thus reducing hydrogen production efficiency and resulting in relatively high electrolytic energy consumption, insufficient for industrial

production requirements [10–12]. To enhance hydrogen production efficiency, industrial electrolytes typically consist of 6 M KOH, with electrolysis conducted at 60 °C [13–15]. Currently, among numerous reported non-metallic materials, nickel–iron-based compounds exhibit notable OER electrocatalytic activity [16–18]. These materials predominantly manifest as metal (hydrogen) oxides (e.g., Ni-Fe-LDH), nitrides (e.g., Ni₃FeN), phosphides (e.g., NiP), selenides (e.g., NiSe), etc. [19–23]. The majority exhibit superior OER catalytic activity compared to noble metal catalysts [24,25]. Nonetheless, synthesis methods reported in the literature mainly involve two or three-step processes, which are cumbersome and inconvenient, resulting in products rarely suitable for high-temperature and strong alkali environments [22,26]. Thus, we developed a one-step synthesis method for a high-temperature and strong alkali-resistant OER catalyst (Fe/Ni)S_x/NF. To distinguish the solution systems, the solution of deionized water and methylbenzene is denoted as DI/MB, the mixture of anhydrous ethanol and methylbenzene as ET/MB, and the catalyst as FeS_x(Y/MB), where X = 0, 1; Y = DI, ET.

This paper's design concept involves dissolving sulfur powder in methylbenzene as the sulfur source, ferric nitrate in ethanol or deionized water as the iron source, and utilizing nickel foam as the nickel source, all through a one-step hydrothermal method for direct material synthesis. The reaction equation can be simply expressed as:



Fe³⁺ exhibits strong oxidizing properties and tends to form Ni/Fe structures on the surfaces of nickel foam. Dissolving Fe(NO₃)₃ in deionized water and adding sulfur-containing toluene resulted in intriguing solution layering phenomena.

Anhydrous ethanol was used instead of deionized water to explore the impact of layered and non-layered solutions on the morphology, structure, and performance of the catalyst. This paper prepared four catalysts, FeS(DI/MB), FeS(ET/MB), Fe(DI/MB), and Fe(ET/MB), using two different solution systems, namely DI/MB and ET/MB. Structural characterization revealed that the FeS(DI/MB) and Fe(DI/MB) catalysts exhibited a dense nanosheet structure, whereas the FeS(ET/MB) and Fe(ET/MB) catalysts lacked such a structure. The lower electronegativity of sulfur facilitates its loading on the edges of Ni/Fe nanosheets during the hydrothermal process, thereby enhancing the material's resistance to strong bases and its catalytic activity. With the KOH concentration increasing from 1 M to 6 M, the OER overpotentials of FeS(DI/MB) were 460 mV and 318 mV at a current density of 500 mA cm⁻², respectively. Additionally, at 6 M 60 °C, FeS(DI/MB) requires only 262 mV to achieve a current density of 500 mA cm⁻². Tested under simulated industrial electrolysis conditions, it was found to exhibit stable performance in high-temperature and strong alkaline environments, indicating its potential for industrial applications. These findings offer novel approaches for NiFeS catalyst synthesis, and further in-depth exploration is anticipated to reveal the excellent catalytic performance of NiFeS catalysts in hydrogen production from electrolyzed water.

2. Results and Discussion

Figure 1 illustrates the preparation of the FeS(DI/MB) electrode via a one-step hydrothermal method. The catalyst was directly synthesized through a one-step hydrothermal method by dissolving sulfur powder in toluene as the sulfur source, iron nitrate in deionized water or anhydrous ethanol as the iron source, and utilizing nickel foam as the nickel source.

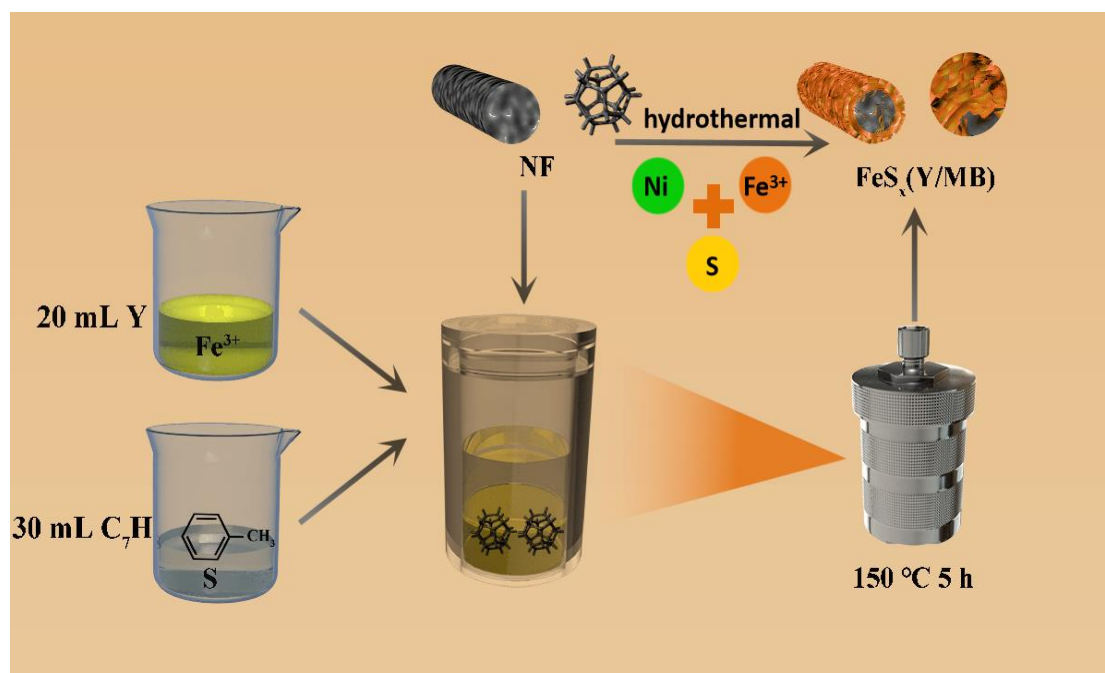


Figure 1. Flowchart for the preparation of $\text{FeS}_x(\text{Y/MB})$, where $X = 0, 1$; $Y = \text{DI, ET}$.

Scanning electron microscopy (SEM) and transmission electron microscopy (TEM) were employed to characterize the morphology and structure of the catalyst. Figure 2a,b reveals that the surface of the $\text{FeS}(\text{DI/MB})$ electrode exhibits a uniformly distributed ultrathin nanosheet array structure, facilitating the provision of abundant active sites and enhancing catalytic performance. Elemental mapping in Figure 2c–g demonstrates the uniform distribution of Ni (d), O (e), Fe (f), and S (g) on the surface of the $\text{FeS}(\text{DI/MB})$ electrode, indicating successful S doping. Figure S1 illustrates that the microscopic morphology of the $\text{FeS}(\text{ET/MB})$ electrodes prepared from the unstratified solution exhibits a distinct granularity, contrasting significantly with the nanosheet structure of $\text{FeS}(\text{DI/MB})$. To further explore the impacts of these two solution systems on catalyst performance, we fabricated $\text{Fe}(\text{DI/MB})$ and $\text{Fe}(\text{ET/MB})$ electrodes using the same method. Figures S2 and S3 reveal that $\text{Fe}(\text{DI/MB})$ also possesses a dense nanosheet structure, while the microstructure of $\text{Fe}(\text{ET/MB})$ is visibly granular, mirroring the SEM images of $\text{FeS}(\text{DI/MB})$ and $\text{FeS}(\text{ET/MB})$. SEM images reveal that the $\text{FeS}(\text{DI/MB})$ and $\text{Fe}(\text{DI/MB})$ electrodes prepared using the DI/MB system exhibit a uniformly distributed ultrathin nanosheet structure, providing more active sites and improved gas permeability.

The structural composition and chemical state of the catalysts were further analyzed by XRD and XPS tests. As shown in Figure 3a, the XRD characteristic peaks of $\text{FeS}(\text{DI/MB})$ correspond to the standard PDF cards of nickel foam and $\text{Fe}_{3.6}\text{Fe}_{0.9}(\text{O, OH, SO}_4)_9$ [27]. The blue vertical lines correspond to the (111), (200), and (220) crystal planes of the standard PDF card (PDF#04-0850) for nickel foam, and the red vertical lines correspond to the (003), (102), and (009) crystal planes of the standard PDF card (PDF #13-0090) for $\text{Fe}_{3.6}\text{Fe}_{0.9}(\text{O, OH, SO}_4)_9$ [27]. The XPS spectra in Figure 3b further confirm the presence of Ni, Fe, S, and O elements in the $\text{FeS}(\text{DI/MB})$ electrode, providing evidence of successful S doping. Figure 3c shows the spectrum of Ni 2p with the characteristic peaks at 875.2 and 857.6 eV corresponding to the two peaks Ni 2p_{1/2} and Ni 2p_{3/2}, respectively, and Sat corresponding to the satellite peaks. These peaks confirm the presence of elemental nickel and indicate that it exists mainly in the Ni^{2+} chemical state [28]. Figure 3d shows the spectrum of Fe 2p and two characteristic peaks can be observed at 725.2 and 713.1 eV, corresponding to Fe 2p_{1/2} and Fe 2p_{3/2}, respectively, indicating that the Fe element on the catalyst surface exists mainly in the form of Fe^{3+} [29]. Figure 3e shows the spectra of O 1s and it can be seen that the O element is present in the form of bonding with metal and hydroxyl groups [30]. This

suggests that the FeS(DI/MB) surface may be rich in highly reactive intermediate states that significantly enhance the OER activity of the catalyst. Figure 3f shows the spectrum of S 2p, again confirming the presence of the S element [31]. In summary, the FeS(DI/MB) electrode exhibits uniform distribution of Fe, Ni, S, and O elements, consistent with the EDX plots of Figure 2c–g.

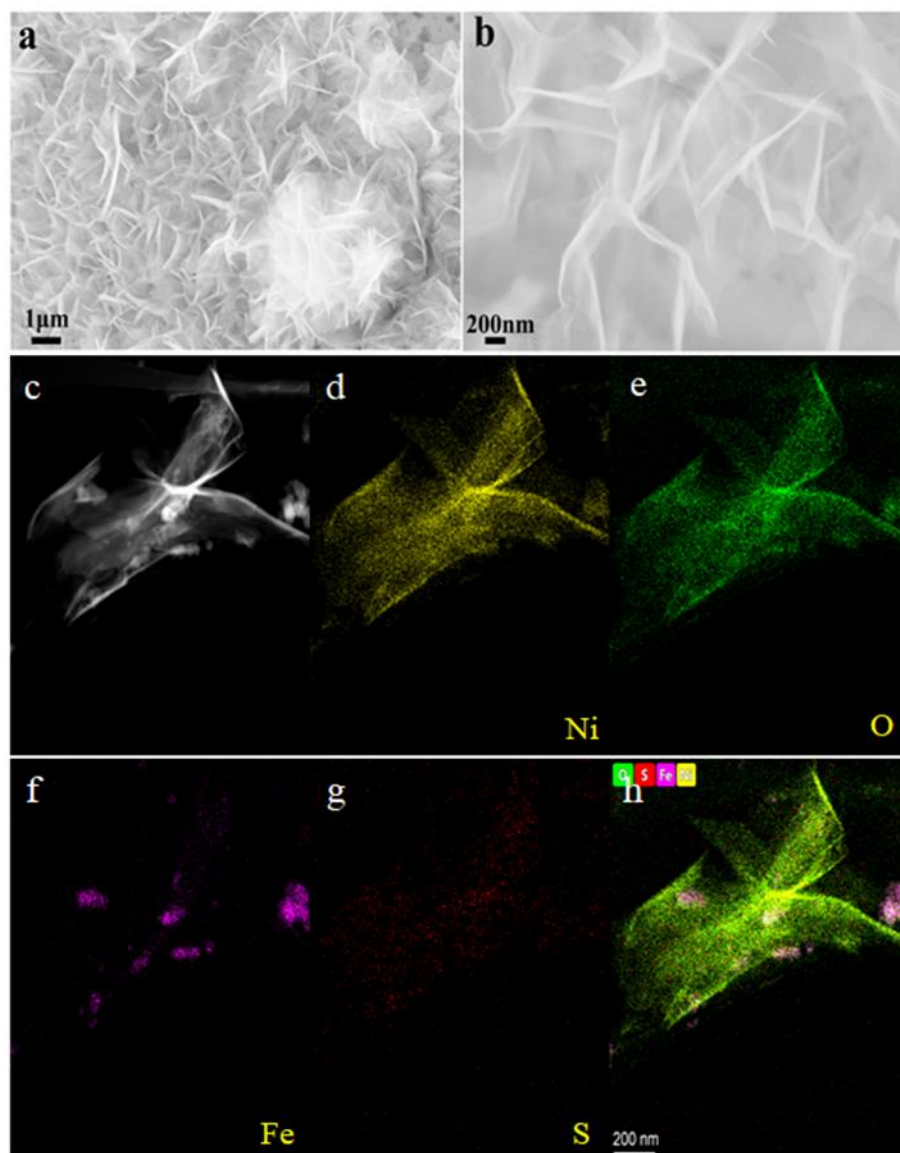


Figure 2. SEM maps of FeS(DI/MB) electrodes (a) 1 μm ; (b) 200 nm; (c) EDX maps of FeS(DI/MB) electrodes; Mapping maps of FeS(DI/MB) electrodes (d) Ni; (e) O; (f) Fe; (g) S; and (h) FeS(DI/MB) electrode HADDF plot.

A three-electrode electrochemical test system was assembled in a 1 M KOH solution to evaluate the OER catalytic activity of FeS(DI/MB), FeS(ET/MB), Fe(DI/MB), Fe(ET/MB) electrodes, and NF. The results are depicted in Figure 4. According to Figure 4a, the FeS(DI/MB) electrode requires an overpotential of 250 mV to achieve a current density of 100 mA cm^{-2} . The current densities achievable by FeS(ET/MB), Fe(DI/MB), Fe(ET/MB), and NF at a 250 mV potential are 46.32, 19.91, 7.736, and 4.28 mA cm^{-2} , respectively. At this overpotential, the current densities of FeS(DI/MB) electrodes surpass those of FeS(ET/MB), Fe(DI/MB), Fe(ET/MB), and NF by factors of 2.16, 5.02, 12.93, and 23.36, respectively. This suggests that S doping enhances the catalytic activity of self-supporting electrodes, facilitating the formation of a uniformly distributed nanosheet structure with

increased active sites and improved oxygen evolution performance. Consequently, the oxygen evolution performance of the nanosheet FeS(DI/MB) electrode surpasses that of the FeS(ET/MB), Fe(DI/MB), Fe(ET/MB) electrodes, and NF. Figure 4b reveals that the Tafel slopes for the FeS(DI/MB), FeS(ET/MB), Fe(DI/MB), and Fe(ET/MB) electrodes are 20.62 mV dec⁻¹, 38.97 mV dec⁻¹, 93.91 mV dec⁻¹, and 51.04 mV dec⁻¹, respectively. A smaller Tafel slope corresponds to a higher reaction rate, indicating a faster reaction. The Tafel slope of the FeS(DI/MB) electrode is significantly smaller than that of the FeS(ET/MB), Fe(DI/MB), and Fe(ET/MB) electrodes. Furthermore, the nanosheet structure formed by S-doped FeNi significantly enhanced the reaction kinetics of the electrode. The stability test of the FeS(DI/MB) electrode is depicted in Figure 4d, showing that the LSV curve remains essentially unchanged after 5000 cycles of CV, demonstrating the excellent stability of the FeS(DI/MB) electrode. The zoomed out graph in Figure 4d indicates that the OER performance of the FeS(DI/MB) electrode decreases almost unchanged after 60 h of continuous i-t testing, further affirming its outstanding stability.

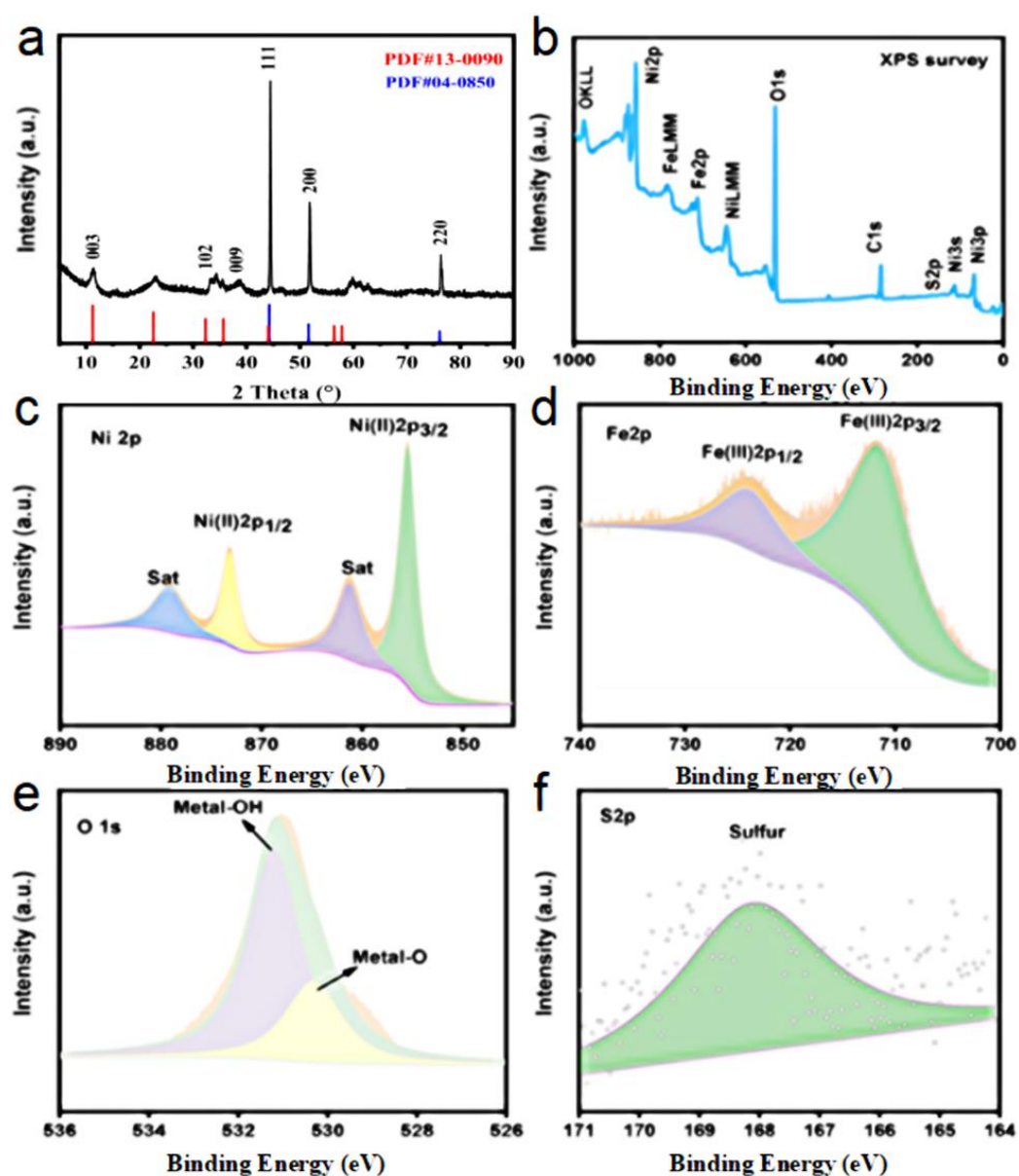


Figure 3. (a) XRD map of FeS(DI/MB) electrode; (b) XPS gross spectrum of FeS(DI/MB) electrode; (c) Ni 2p; (d) Fe 2p; (e) O 1s; and (f) S 2p.

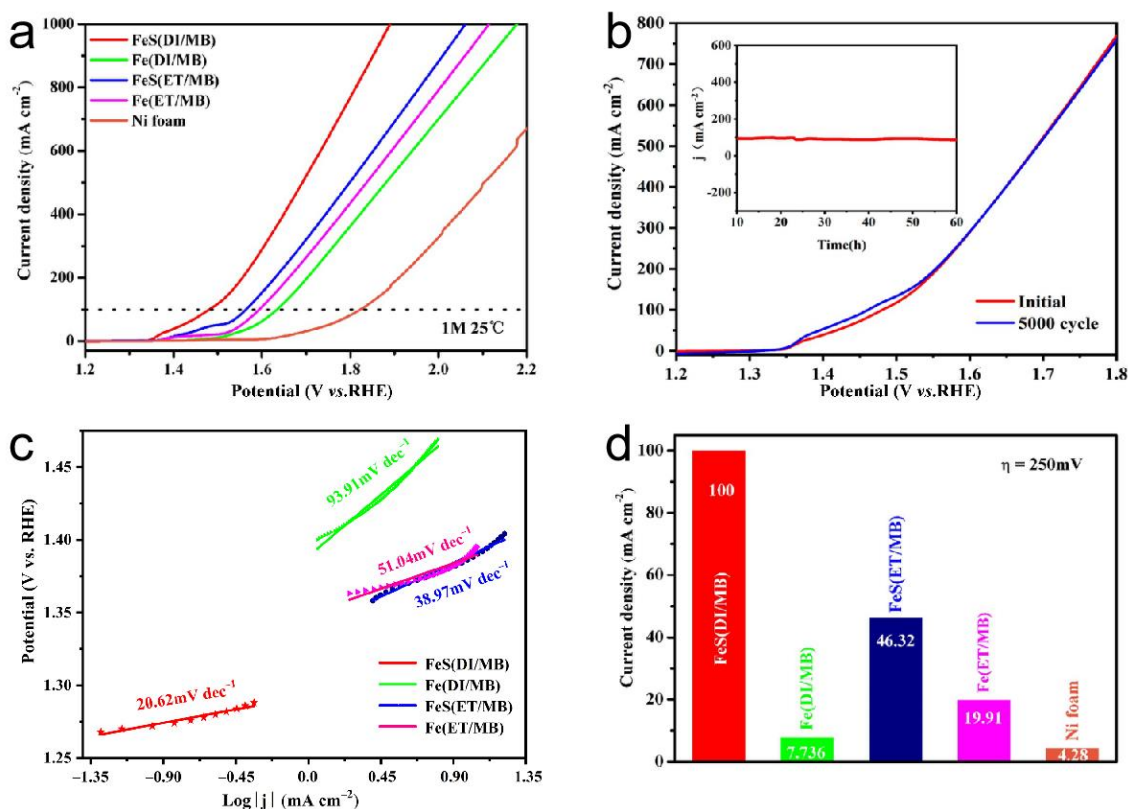


Figure 4. (a) LSV curves, (b) Tafel slopes, (c) current densities at overpotential $\eta = 250$ mV of FeS(DI/MB), FeS(ET/MB), Fe(DI/MB), Fe(ET/MB), and nickel (Ni foam) electrodes. (d) Stability tests of FeS(DI/MB). Tested at a room temperature of 25 °C and 1 M KOH.

In order to assess the relative electrochemically active surface area of the electrodes, the electrochemical double-layer capacitance (C_{dl}) was estimated by cyclic voltammetry (CV) [32]. Figure S5 summarizes the converted C_{dl} values of each electrode. It is evident that the C_{dl} value of the FeS(DI/MB) electrode (10.24 mF cm^{-2}) is significantly larger than that of the FeS(ET/MB) electrode (9.16 mF cm^{-2}), the Fe(DI/MB) electrode (5.15 mF cm^{-2}), and the Fe(ET/MB) electrode (9 mF cm^{-2}). This suggests that the FeS(DI/MB) electrode has more active sites. The electrochemically active surface area (ECSA) is closely related to C_{dl} . The larger the C_{dl} value, the greater the ECSA value, indicating that the electrochemically effective active surface area of the catalyst is larger, and bubbles are more conducive to separation from the electrode surface, resulting in better OER catalytic activity [33].

The electrolyte alkalinity was increased from 1 M KOH to 6 M KOH, while maintaining a temperature of 25 °C. A three-electrode system was assembled to evaluate the OER catalytic activity of the FeS(DI/MB), FeS(ET/MB), Fe(DI/MB), Fe(ET/MB) electrodes, and the NF. The results are depicted in Figure 5. As can be seen in Figure 5a, from the perspective of whether the solution is layered or not, the OER catalysis of the FeS(DI/MB) electrode is superior to that of FeS(ET/MB), and the OER performance of Fe(DI/MB) is superior to that of Fe(ET/MB). From the point of view of whether vulcanization takes place or not, the OER catalytic performance of the FeS(DI/MB) electrode is superior to that of Fe(DI/MB), and the OER catalytic performance of the FeS(ET/MB) electrode is superior to that of Fe(ET/MB). The Tafel slope also confirms the above relationship, as shown in Figure 5b. The Tafel slope of FeS(DI/MB) is $18.33 \text{ mV dec}^{-1}$, which is significantly smaller than the 34.92 , 28.01 , and $50.14 \text{ mV dec}^{-1}$ of FeS(ET/MB), Fe(DI/MB), and Fe(ET/MB). This indicates that FeS(DI/MB) still exhibits excellent reaction kinetics in a strong alkaline environment of 6 M. As can be seen from Figure 5c, the FeS(DI/MB) catalytic electrode requires an overpotential of 318 mV to release 500 mA cm^{-2} under this test condition, and the current densities that can be achieved by FeS(ET/MB), Fe(DI/MB), Fe(ET/MB), and nickel (Ni foam) in empty

foam at this potential are 242.56, 250.84, 140.68, and 5.91 mA cm⁻², respectively. At the same overpotential, the current density of FeS(DI/MB) is 2.06, 1.99, 3.55, and 84.60 times higher than that of FeS(ET/MB), Fe(DI/MB), Fe(ET/MB), and NF. Figure 5d shows the stability test of the FeS(DI/MB) electrodes in 6 M KOH. After 5000 cycles of CV, the LSV curve remains basically unchanged, indicating that FeS(DI/MB) batteries have excellent stability, which proves that the FeS(DI/MB) electrode still has excellent stability in a strong alkaline environment of 6 M KOH.

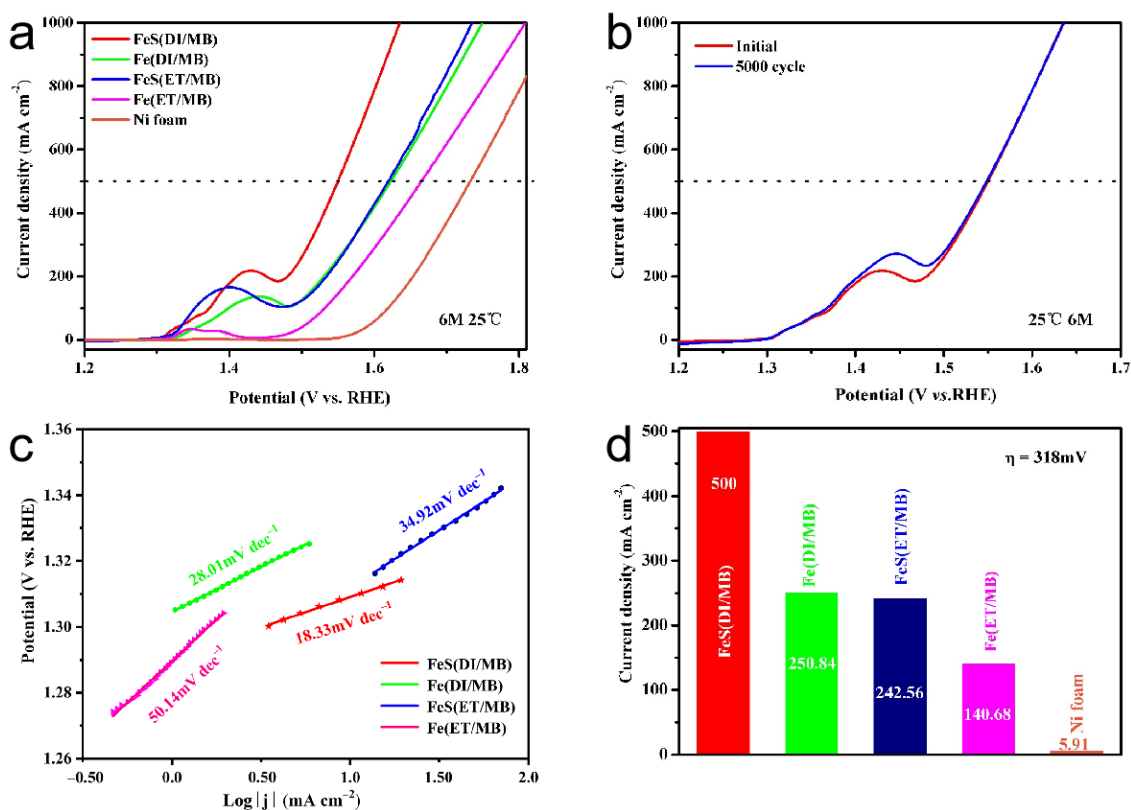


Figure 5. (a) LSV curves, (b) Tafel slopes, (c) current densities at overpotential $\eta = 318$ mV of FeS(DI/MB), FeS(ET/MB), Fe(DI/MB), Fe(ET/MB), and nickel (Ni foam) electrodes. (d) Stability tests of FeS(DI/MB). Tested at a room temperature of 25 °C and 6 M KOH.

The electrochemical double-layer capacitance (C_{dl}) was estimated using cyclic voltammetry (CV) to assess the relative electrochemically active surface area of the electrodes in a high-concentration electrolyte. Figure S7 illustrates that the C_{dl} value for the FeS(DI/MB) electrode (15.18 mF cm⁻²) significantly exceeds those of the FeS(ET/MB) electrode (14.16 mF cm⁻²), the Fe(DI/MB) electrode (9.74 mF cm⁻²), and the Fe(ET/MB) electrode (7.92 mF cm⁻²), suggesting a higher number of active sites on the FeS(DI/MB) electrode.

Further, the simulated industrial electrolysis conditions were tested, the alkalinity of the electrolyte was kept constant on the basis of the former experiment (6 M KOH), the ambient temperature was increased from a room temperature of 25 °C to 60 °C: i.e., the tests were carried out at high temperatures and in strong alkaline conditions, and a three-electrode system was constructed for evaluating the catalytic activity of FeS(DI/MB), FeS(ET/MB), Fe(DI/MB), Fe(ET/MB) electrodes, and NF OER, and the results of the tests are shown in Figure 6. As can be seen in Figure 6a, from the perspective of whether the solution is layered or not, the OER catalysis of the FeS(DI/MB) electrode is superior to that of FeS(ET/MB), and the OER performance of the Fe(DI/MB) is superior to that of the Fe(ET/MB). The OER catalytic performance of the FeS(DI/MB) electrode was superior to that of the Fe(DI/MB) electrode in terms of whether it was sulfated or not. And the OER performance of the FeS(ET/MB) electrode is superior to the Fe(ET/MB) electrode. Their Tafel slopes (b) similarly corroborate the above relationship. Figure 6b shows that the

Tafel slope of FeS(DI/MB) is $15.31 \text{ mV dec}^{-1}$, which is much smaller than the 28.01, 29.14, and $77.57 \text{ mV dec}^{-1}$ of FeS(ET/MB), Fe(DI/MB), and Fe(ET/MB). This indicates that the FeS(DI/MB) electrode still exhibits excellent reaction kinetics under 6 M KOH and 60°C conditions. As can be seen from Figure 6c, the FeS(DI/MB) catalytic electrode requires an overpotential of 262 mV to release a current density of 500 mA cm^{-2} under simulated industrial electrolysis conditions. At this potential, the current densities of FeS(ET/MB), Fe(DI/MB), Fe(ET/MB), and NF were 250.84, 242.56, 140.68, and 26.95 mA cm^{-2} , respectively. At the same overpotential, the current density of FeS(DI/MB) is 1.99, 2.06, 3.55, and 18.55 times higher than that of FeS(ET/MB), Fe(DI/MB), Fe(ET/MB), and NF. As shown in Figure 6d, the LSV curves before and after 5000 CV cycles of charge discharge tests are basically consistent, indicating that the FeS(DI/MB) electrode containing FeNi sulfide catalyst has very high electrochemical stability under simulated industrial electrolysis conditions (6 M KOH, 60°C). In summary, FeS(DI/MB) electrodes exhibit excellent OER catalytic activity and stability under simulated industrial electrolysis conditions, and their preparation process is simple and low-cost, with good industrial application prospects.

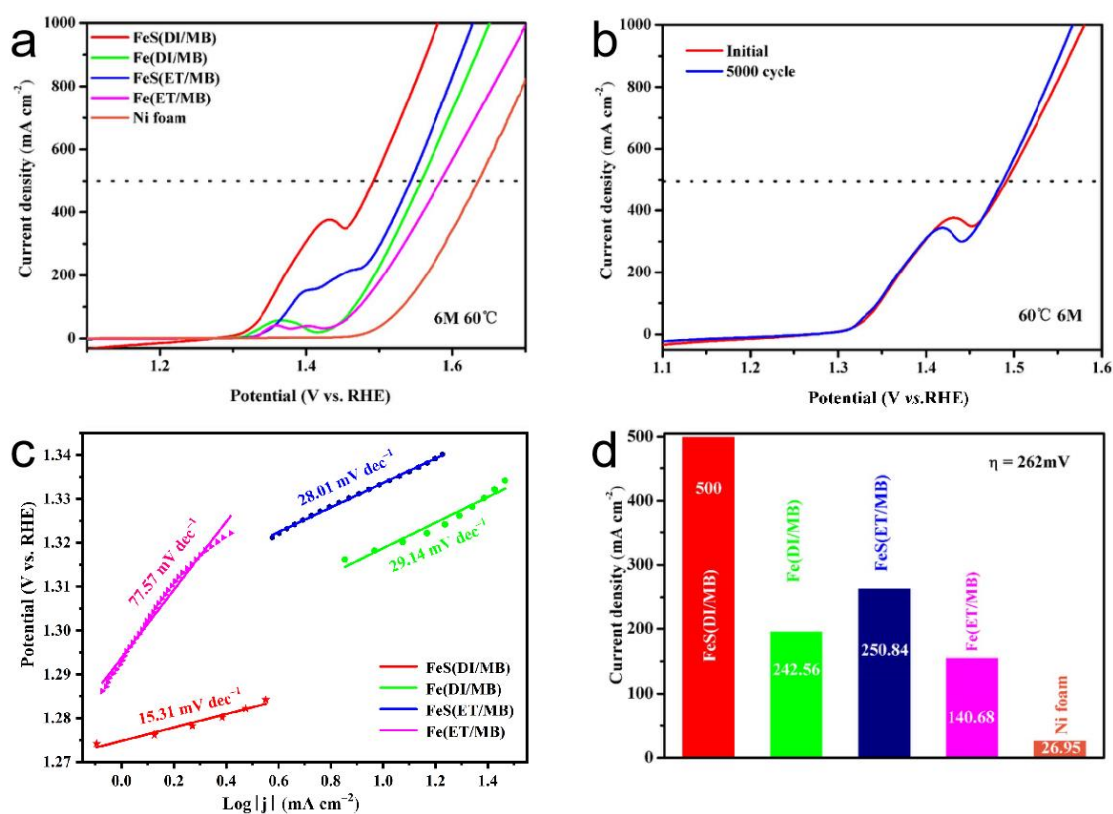


Figure 6. (a) LSV curves, (b) Tafel slopes, (c) current densities at overpotential $\eta = 262 \text{ mV}$ of FeS(DI/MB), FeS(ET/MB), Fe(DI/MB), Fe(ET/MB), and nickel (Ni foam) electrodes. (d) Stability tests of FeS(DI/MB). Tested under simulated industrial conditions (6 M KOH, 60°C).

3. Materials and Methods

3.1. Chemicals and Materials

The ferric nitrate nonahydrate ($\text{Fe}(\text{NO}_3)_3 \cdot 9\text{H}_2\text{O}$, 98%), hydrochloric acid (HCl, 37 wt%), sublimated sulfur (S), methylbenzene (C_6H_6), and potassium hydroxide (KOH, $\geq 98\%$) were prepared from Aladdin Reagent Co., Ltd., Shanghai, China. The Ni foam was obtained from Kunshan Jiayisheng Electronics Co., Ltd., Kunshan, China. The anhydrous ethanol was purchased from Tianjin Kaitong Chemical Reagent Co., Ltd., Tianjin, China.

3.2. Synthesis of FeS(DI/MB)

The nickel foam (NF), measuring 0.5 cm × 0.5 cm × 0.01 cm, underwent successive ultrasonic cleaning with 3 M HCl, anhydrous ethanol, and deionized water for 30 min to eliminate the inert oxide film from the surface. After cleaning, dry the nickel foam base in an oven at 60 °C to obtain the prefabricated nickel foam base.

Employ an electronic balance to precisely measure 0.30 g of ferric nitrate nonahydrate dissolved in 20 mL of deionized water, followed by 0.05 g of sublimated sulfur dissolved in 30 mL of methylbenzene solution. Stir each solution individually. Subsequently, combine the two solutions to form a layered solution, with the organic and aqueous layers remaining immiscible. Submerge the prepared nickel foam sheet vertically into the lower layer of the aforementioned layered solution, then subject it to calcination in a muffle furnace at 150 °C for 5 h. Following cooling, wash the catalyst with distilled water and dry it to obtain the nickel iron sulfide catalyst prepared from the layered solution system, designated as FeS(DI/MB).

3.3. Synthesis of FeS(ET/MB)

Utilize an electronic balance to precisely measure 0.30 g of ferric nitrate nonahydrate dissolved in 20 mL of anhydrous ethanol, followed by 0.05 g of sublimated sulfur dissolved in 30 mL of methylbenzene solution. Stir each solution individually. Subsequently, combine the two solutions to obtain a homogeneous mixture. Submerge the pretreated nickel foam sheet vertically into the aforementioned mixed solution, then subject it to calcination in a muffle furnace at 150 °C for 5 h. After cooling, wash it with distilled water and dry it to obtain nickel–iron sulfide catalysts prepared from the layered solution system, designated as FeS(ET/MB).

3.4. Synthesis of Fe(DI/MB)

Accurately weigh 0.30 g of ferric nitrate hydrate using an electronic balance, then dissolve it in 20 mL of distilled water. Next, weigh 30 mL of methylbenzene solution and combine it with the previously prepared solution to form a layered solution where the organic and aqueous layers remain immiscible. Vertically place the pretreated nickel foam sheet in the lower layer of the layered solution mentioned above, then calcine it in a muffle furnace at 150 °C for 5 h. After cooling, wash the catalyst with distilled water and dry it to obtain the nickel–iron sulfide catalyst prepared from the layered solution system, designated as Fe(DI/MB).

3.5. Synthesis of Fe(ET/MB)

Accurately weigh 0.30 g of ferric nitrate hydrate using an electronic balance, then dissolve it in 20 mL of distilled water. Next, weigh 30 mL of methylbenzene solution and combine it with the previously prepared solution to form a mixed solution. Vertically place the pretreated nickel foam sheet in the lower layer of the mixed solution mentioned above, and then calcine it in a muffle furnace at 150 °C for 5 h. After cooling, wash the catalyst with distilled water and dry it to obtain the nickel–iron–sulfide catalyst prepared from the mixed solution, designated as Fe(DI/MB).

3.6. Electrochemical Measurements

All electrochemical measurements are carried out at the CHI440 electrochemical workstation under ambient conditions. A standard three-electrode system was adopted for OER. The electrodes (FeS(DI/MB), FeS(ET/MB), Fe(DI/MB), and Fe(ET/MB)) prepared in the above steps were used as working electrodes (0.25 cm^{−2}), and carbon rod and Hg/HgO were used as counter and reference electrodes, respectively. The electrochemical test was performed at room temperature, 1 M and 6 M KOH. The potential obtained by calibration with a reversible hydrogen electrode (RHE) and the electrochemical test of the overall water

decomposition were performed in a two-electrode system. The reversible hydrogen (RHE) electrode was used as a reference scale through the potential conversion equation:

$$E_{\text{RHE}} = E_{\text{Hg/HgO}} + 0.098 + 0.059 \times \text{pH} \quad (\text{pH} = 14.778) \quad (3)$$

Linear scanning voltammetry (LSV) was measured at 1 mV s^{-1} . Electrochemical impedance spectra (EIS) were tested in the frequency range of 100 kHz to 10 mHz. The electrochemical double-layer capacitance (C_{dl}) values were obtained by testing cyclic voltammetry (CV) at scan rates from 20 to 200 mV s^{-1} . Cyclic stability tests were performed for 5000 cycles at a scan rate of 50 mV s^{-1} . Chronopotentiometric stability tests were performed at a constant current density of 100 mA cm^{-2} .

3.7. Characterization Tests

Using an X-ray diffractometer ($30\text{--}80^\circ$), the crystal characteristics of the electrocatalysts as-prepared were examined. Transmission electron microscopy (TEM) and field emission scanning electron microscopy (SEM) were used to observe morphology and microstructure at a 20 kV accelerating voltage. The VG-ESCA Scientific Theta Probe spectrometer and Al-K α Perform X-ray photoelectron spectroscopy (XPS) were used with a beam (1486.6 eV) to analyze the types of elements on the surface of the sample and to quantitatively and qualitatively analyze the chemical states of the elements contained within.

4. Conclusions

To sum up, through the step-by-step change in the test environment from 25°C , 1 M KOH to the chamber and finally to the simulated industrial electrolysis conditions, a high temperature of 60°C and a strong alkali of 6 M KOH, it is concluded that increasing the alkaline electrolyte and temperature are conducive to water decomposition. The OER performance of the FeS(DI/MB) catalytic electrode prepared with stratified solution system (DI/MB) is better than that of FeS(ET/MB) prepared with unstratified solution system (ET/MB), and the OER performance of Fe(DI/MB) is better than that of Fe(ET/MB). The results show that the catalyst prepared by the layered system has better reaction kinetics and is more suitable for water electrolysis. The OER performance of FeS(DI/MB) is better than that of Fe(DI/MB), and the OER performance of FeS(ET/MB) is better than that of Fe(ET/MB), indicating that the performance becomes better after vulcanization. The test also shows excellent electrochemical stability under simulated industrial electrolysis conditions, which is suitable for use as an industrial electrolytic water catalyst. This provides a new research idea for the research of electrolytic water, that is, to increase the electrochemical performance of the catalyst by changing the testing environment of the electrolyte.

Supplementary Materials: The following supporting information can be downloaded at: <https://www.mdpi.com/article/10.3390/catal14050324/s1>, Figure S1. SEM images of FeS(ET/MB) electrodes. (a) $1 \mu\text{m}$; (b) 200 nm ; Figure S2. SEM images of Fe(DI/MB) electrodes. (a) $1 \mu\text{m}$; (b) 200 nm ; Figure S3. SEM images of Fe(ET/MB) electrodes. (a) $1 \mu\text{m}$; (b) 200 nm ; Figure S4. CV diagram of catalyst in 1 M KOH and at 25°C . FeS(DI/MB), Fe(DI/MB), FeS(ET/MB), Fe(ET/MB); Figure S5. C_{dl} plots of FeS(DI/MB), Fe(DI/MB), FeS(ET/MB), Fe(ET/MB); Figure S6. CV diagram of catalyst in 6 M KOH and at 25°C . FeS(DI/MB), Fe(DI/MB), FeS(ET/MB), Fe(ET/MB); Figure S7. C_{dl} plots of FeS(DI/MB), Fe(DI/MB), FeS(ET/MB), Fe(ET/MB).

Author Contributions: Conceptualization: J.Z. and F.G.; methodology, J.W.; software, J.W.; validation, J.Z. and L.F.; formal analysis, J.W. and L.F.; investigation, Y.W. and S.S. (Shan Song); resources, J.Z. and F.G.; data curation, J.W., Z.Z. and S.S. (Shengwei Sun); writing—original draft preparation, J.W. and L.F.; writing—review and editing, Z.Z. and Y.Z.; visualization, J.W.; supervision, J.Z. and F.G.; project administration, F.G.; funding acquisition, F.G. All authors have read and agreed to the published version of the manuscript.

Funding: This research was supported by National Natural Science Foundation of China (Grant Nos. 21875205, 22209141) and Hebei Province Foundation for the National Natural Science Foundation (Grant Nos. 206Z4404G, B2021203016, 236Z4405G).

Data Availability Statement: All the relevant data used in this study have been provided in the form of figures and tables in the published article, and all data provided in the present manuscript are available upon reasonable request.

Conflicts of Interest: The authors declare no conflicts of interest.

References

1. Li, Y.; Jiang, K.; Yang, J.; Zheng, Y.; Hübner, R.; Ou, Z.; Dong, X.; He, L.; Wang, H.; Li, J.; et al. Tungsten Oxide/Reduced Graphene Oxide Aerogel with Low-Content Platinum as High-Performance Electrocatalyst for Hydrogen Evolution Reaction. *Small* **2021**, *17*, 2102159. [[CrossRef](#)] [[PubMed](#)]
2. Yu, H.; Xie, S.; Yang, J.; Lv, J.; Tan, W.; Yin, J.; Wang, J.; Zhao, M.; Wang, C.; Zhang, M.; et al. Co₃Fe₇/Mo₂C co-embedded in N-codoped porous carbon with accelerated kinetics for OER and HER. *Colloids Surf. A Physicochem. Eng. Aspects* **2022**, *645*, 128953. [[CrossRef](#)]
3. Zhang, J.; Lian, J.; Jiang, Q.; Wang, G. Boosting the OER/ORR/HER activity of Ru-doped Ni/Co oxides heterostructure. *Chem. Eng. J.* **2022**, *439*, 135634. [[CrossRef](#)]
4. Liu, H.; Zhang, Y.; Ge, R.; Cairney, J.M.; Zheng, R.; Khan, A.; Li, S.; Liu, B.; Dai, L.; Li, W. Tailoring the electronic structure of Ni₅P₄/Ni₂P catalyst by Co₂P for efficient overall water electrolysis. *ApEn* **2023**, *349*, 121582. [[CrossRef](#)]
5. Zhou, P.; Hai, G.; Zhao, G.; Li, R.; Huang, X.; Lu, Y.; Wang, G. CeO₂ as an “electron pump” to boost the performance of Co₄N in electrocatalytic hydrogen evolution, oxygen evolution and biomass oxidation valorization. *Appl. Catal. B Environ.* **2023**, *325*, 122364. [[CrossRef](#)]
6. Zhang, R.; Liu, W.; Zhang, F.-M.; Yang, Z.-D.; Zhang, G.; Zeng, X.C. COF-C₄N Nanosheets with uniformly anchored single metal sites for electrocatalytic OER: From theoretical screening to target synthesis. *Appl. Catal. B Environ.* **2023**, *325*, 122366. [[CrossRef](#)]
7. Ahasan Habib, M.; Mandavkar, R.; Lin, S.; Burse, S.; Khalid, T.; Hasan Joni, M.; Jeong, J.-H.; Lee, J. Ni-B-P micro spheres for superior water splitting OER electrocatalyst satisfying industrial operational requirement. *Chem. Eng. J.* **2023**, *462*, 142177. [[CrossRef](#)]
8. Chen, L.; Wang, H.Y.; Tian, W.W.; Wang, L.; Sun, M.L.; Ren, J.T.; Yuan, Z.Y. Enabling Internal Electric Field in Heterogeneous Nanosheets to Significantly Accelerate Alkaline Hydrogen Electrocatalysis. *Small* **2023**, *20*, 2307252. [[CrossRef](#)] [[PubMed](#)]
9. Hemmati, K.; Kumar, A.; Jadhav, A.R.; Moradlou, O.; Moshfegh, A.Z.; Lee, H. Nanorod Array-Based Hierarchical NiO Microspheres as a Bifunctional Electrocatalyst for a Selective and Corrosion-Resistance Seawater Photo/Electrolysis System. *ACS Catal.* **2023**, *13*, 5516–5528. [[CrossRef](#)]
10. Liu, Y.; Zhou, B.; Zhang, Y.; Xiao, W.; Li, B.; Wu, Z.; Wang, L. In situ synthesis of two-dimensional graphene-like nickel-molybdenum nitride as efficient electrocatalyst towards water-splitting under large-current density. *J. Colloid Interface Sci.* **2023**, *637*, 104–111. [[CrossRef](#)]
11. Shen, X.; Wei, X.; Wang, T.; Li, S.; Li, H. Polypyrrole embedded in nickel-cobalt sulfide nanosheets grown on nickel particles passivated silicon nanowire arrays for high-performance supercapacitors. *Chem. Eng. J.* **2023**, *461*, 141745. [[CrossRef](#)]
12. Wang, X.; Yu, X.; Bai, J.; Yuan, G.; He, P.; Zhu, Y.; Wu, S.; Qin, F.; Ren, L. Interface engineering assisted Fe-Ni₃S₂/Ni₂P heterostructure as a high-performance bifunctional electrocatalyst for OER and HER. *Electrochim. Acta* **2023**, *458*, 142524. [[CrossRef](#)]
13. Zhang, H.; Qian, G.; Yu, T.; Chen, J.; Luo, L.; Yin, S. Interface Engineering of Ni₃Fe and FeV₂O₄ Coupling with Carbon-Coated Mesoporous Nanosheets for Boosting Overall Water Splitting at 1500 mA cm⁻². *ACS Sustain. Chem. Eng.* **2021**, *9*, 8249–8256. [[CrossRef](#)]
14. Chen, J.; Wang, Y.; Qian, G.; Yu, T.; Wang, Z.; Luo, L.; Shen, F.; Yin, S. In situ growth of volcano-like FeIr alloy on nickel foam as efficient bifunctional catalyst for overall water splitting at high current density. *Chem. Eng. J.* **2021**, *421*, 129892. [[CrossRef](#)]
15. Qian, G.; Chen, J.; Yu, T.; Luo, L.; Yin, S. N-Doped Graphene-Decorated NiCo Alloy Coupled with Mesoporous NiCoMoO Nano-sheet Heterojunction for Enhanced Water Electrolysis Activity at High Current Density. *Nano-Micro Lett.* **2021**, *13*, 77. [[CrossRef](#)]
16. Liu, X.; Guo, X.; Gong, M.; Zhao, T.; Zhang, J.; Zhu, Y.; Wang, D. Regulated iron corrosion towards fabricating large-area self-supporting electrodes for an efficient oxygen evolution reaction. *J. Mater. Chem. A* **2021**, *9*, 23188–23198. [[CrossRef](#)]
17. Zhao, Y.; Gao, Y.; Chen, Z.; Li, Z.; Ma, T.; Wu, Z.; Wang, L. Trifling Pt coupled with NiFe hydroxide synthesized via corrosion engineering to boost the cleavage of water molecule for alkaline water-splitting. *Appl. Catal. B Environ.* **2021**, *297*, 120395. [[CrossRef](#)]
18. Jang, M.J.; Yang, S.H.; Park, M.G.; Jeong, J.; Cha, M.S.; Shin, S.-H.; Lee, K.H.; Bai, Z.; Chen, Z.; Lee, J.Y.; et al. Efficient and Durable Anion Exchange Membrane Water Electrolysis for a Commercially Available Electrolyzer Stack using Alkaline Electrolyte. *ACS Energy Lett.* **2022**, *7*, 2576–2583. [[CrossRef](#)]
19. Park, Y.H.; Patil, S.B.; Jin, X.; Hwang, S.-J. High efficacy of substrate dimensionality control in optimizing the specific capacitance and phase stability of hybridized nanostructures. *Nano Energy* **2023**, *113*, 108566. [[CrossRef](#)]

20. Yu, L.; Zhang, G.; Chen, H.; Zeng, J.; Liu, Y.; Yang, Q.; Zhong, L.; Qiu, Y. Ultrathin hollow hemisphere-carbon-anchored Ni₃FeN nanoparticles as nanoreactors facilitating the formation of NiCx with long-term durability for the oxygen evolution reaction. *J. Mater. Chem. A* **2022**, *10*, 7911–7919. [[CrossRef](#)]
21. Jeong, D.I.; Choi, H.W.; Woo, S.; Yoo, J.H.; Kang, D.; Kim, S.; Lim, B.; Kim, J.H.; Kim, S.-W.; Kang, B.K.; et al. Electronic structure modification and N-doped carbon shell nanoarchitectonics of Ni₃FeN@NC for overall water splitting performance evaluation. *J. Mater. Chem. A* **2022**, *10*, 16704–16713. [[CrossRef](#)]
22. Xing, Y.; Liu, S.; Liu, Y.; Xiao, X.; Li, Y.; Wang, Z.; Hu, Y.; Xin, B.; Wang, H.; Wang, C. Construction of nickel phosphide/iron oxyhydroxide heterostructure nanoparticles for oxygen evolution. *Nano Energy* **2024**, *123*, 109402. [[CrossRef](#)]
23. Xu, J.; Ruan, J.; Jian, Y.; Lao, J.; Li, Z.; Xie, F.; Jin, Y.; Yu, X.; Lee, M.-H.; Wang, Z.; et al. Cobalt-Doping Induced Formation of Five-Coordinated Nickel Selenide for Enhanced Ethanol Assisted Overall Water Splitting. *Small* **2024**, *20*, 2305905. [[CrossRef](#)]
24. Xue, H.; Yang, T.; Zhang, Z.; Zhang, Y.; Geng, Z.; He, Y. Stimulate the hidden catalysis potential and exposure of nickel site in NiSe@CNTs result in ultra-high HER/OER activity and stability. *Appl. Catal. B Environ.* **2023**, *330*, 122641. [[CrossRef](#)]
25. Chen, H.; Gao, R.-T.; Chen, H.; Yang, Y.; Wu, L.; Wang, L. Ruthenium and Silver Synergetic Regulation NiFe LDH Boosting Long-Duration Industrial Seawater Electrolysis. *Adv. Funct. Mater.* **2024**, 2315674. [[CrossRef](#)]
26. He, X.; Han, X.; Zhou, X.; Chen, J.; Wang, J.; Chen, Y.; Yu, L.; Zhang, N.; Li, J.; Wang, S.; et al. Electronic modulation with Pt-incorporated NiFe layered double hydroxide for ultrastable overall water splitting at 1000 mA cm⁻². *Appl. Catal. B Environ.* **2023**, *331*, 122683. [[CrossRef](#)]
27. Wang, W.; Dong, Q.; Qiu, H.; Li, H.; Mao, Y.; Liu, Y.; Gong, T.; Xiang, M.; Huang, Y.; Wang, C.; et al. Rapid reactivation of aged NZVI/GO by *Shewanella* CN32 for efficient removal of tetrabromobisphenol A and associated reaction mechanisms. *J. Clean. Prod.* **2022**, *333*, 130215. [[CrossRef](#)]
28. Wang, H.; Zhan, W.; Yu, H.; Jiang, S.; Wang, B.; Deng, K.; Wang, Z.; Xu, Y.; Wang, L. Nitrogen-doped Ni₃P–NiMoO₄ heterostructure arrays for coupling hydrogen production with polyethylene terephthalate plastic electro-recycling. *Mater. Today Phys.* **2023**, *37*, 101192. [[CrossRef](#)]
29. Mai, W.; Cui, Q.; Zhang, Z.; Wen, D.; Tian, L.; Hu, W. Coaxial Ni₃S₂@CoMoS₄/NiFeOOH nanorods for energy-saving water splitting and urea electrolysis. *Int. J. Hydrogen Energy* **2021**, *46*, 24078–24093. [[CrossRef](#)]
30. Dong, J.; Wang, Y.; Jiang, Q.; Nan, Z.-A.; Fan, F.R.; Tian, Z.-Q. Charged droplet-driven fast formation of nickel–iron (oxy)hydroxides with rich oxygen defects for boosting overall water splitting. *J. Mater. Chem. A* **2021**, *9*, 20058–20067. [[CrossRef](#)]
31. Zang, Z.; Guo, Q.; Li, X.; Cheng, Y.; Li, L.; Yu, X.; Lu, Z.; Yang, X.; Zhang, X.; Liu, H. Construction of a S and Fe co-regulated metal Ni electrocatalyst for efficient alkaline overall water splitting. *J. Mater. Chem. A* **2023**, *11*, 4661–4671. [[CrossRef](#)]
32. Li, W.; Sun, Z.; Ge, R.; Li, J.; Li, Y.; Cairney, J.M.; Zheng, R.; Li, Y.; Li, S.; Li, Q.; et al. Nanoarchitectonics of La-Doped Ni₃S₂/MoS₂ Heterostructural Electrocatalysts for Water Electrolysis. *Small Struct.* **2023**, *4*, 2300175. [[CrossRef](#)]
33. Kong, D.; Wang, Y.; Huang, S.; Lim, Y.V.; Wang, M.; Xu, T.; Zang, J.; Li, X.; Yang, H.Y. Defect-Engineered 3D hierarchical NiMo₃S₄ nanoflowers as bifunctional electrocatalyst for overall water splitting. *J. Colloid Interface Sci.* **2022**, *607*, 1876–1887. [[CrossRef](#)]

Disclaimer/Publisher’s Note: The statements, opinions and data contained in all publications are solely those of the individual author(s) and contributor(s) and not of MDPI and/or the editor(s). MDPI and/or the editor(s) disclaim responsibility for any injury to people or property resulting from any ideas, methods, instructions or products referred to in the content.